PERGAMON

International Journal of Heat and Mass Transfer 43 (2000) 2375–2393

International Journal of HEAT and MASS TRANSFER

www.elsevier.com/locate/ijhmt

Direct and large-eddy simulation of the transition of two- and three-dimensional plane plumes in a confined enclosure

Rob J.M. Bastiaans[a,*], C.C.M. Rindt[a], F.T.M. Nieuwstadt[b], A.A. van Steenhoven[a]

[a] *J.M. Burgers Centre for Fluid Dynamics, Department of Mechanical Engineering, Eindhoven University of Technology, P.O. Box 513, nl-5600 MB Eindhoven, The Netherlands*

[b] *J.M. Burgers Centre for Fluid Dynamics, Delft University of Technology, Laboratory of Aero and Hydro-dynamics, Rotterdamseweg 145, nl-2628 AL Delft, The Netherlands*

Received 19 February 1999; received in revised form 3 May 1999

Abstract

We investigate here, the free convection flow induced by a line heat source in a confined geometry. The buoyancy forcing of this flow can be characterized by a Rayleigh number, Ra, which is chosen in the range where an intermittent spatial transition from laminar to turbulent flow takes place. The objective of the study is to explore this flow with help of numerical simulations. We restrict ourselves to the case of an air flow with $Ra = 10^{10}$. For the numerical simulation techniques, we employ Direct Numerical Simulation (DNS) and Large-Eddy Simulation (LES). With help of DNS we consider first, a 2D representation of this flow at a resolution of 195^2 which is found to be sufficient to represent the heat source and its resulting flow. Next, we consider the 3D case at a resolution of 195^3. The 3D simulation reveals a symmetrical time mean recirculation which covers the domain above the heat source. This large scale circulation is driven by the small scale laminar plume generated by the heat source and which breaks down into turbulence. The flow is found to be essentially 3D, especially near the top wall. No clear turbulent inertial range is present. A LES for the same flow has been carried out at a resolution of 45^3. The comparison of the les results with the DNS data has been used to investigate the performance of several sub-grid models. It turns out that simple equilibrium sub-grid models perform fairly well in estimating the statistics of the flow.

Keywords: Plume; Transition; DNS; LES; SGS models

1. Introduction

A free convection plume is an example of a very complex flow despite its simple geometry. The case of a fully developed buoyant plume in unbounded space is well documented in the literature, both for a plume originating from a point source as well as for a plane plume generated by a line source. Here, we will focus on the latter case. The laminar variant of an unbounded plane plume is described by Gebhart et al. [8] in terms of a similarity solution of the governing equations. The stability of a plane

* Corresponding author. Tel.: +31-40-247-4836; fax: +31-40-243-3445.

E-mail address: r.j.m.bastiaans@wtb.tue.nl (R.J.M. Bastiaans).

0017-9310/00/$ - see front matter
PII: S0017-9310(99)00302-6

Nomenclature

a	amplitude
e_{sgs}	sub-grid kinetic energy
f	any quantity
$\bar{f}, \hat{f}$	filtered quantity
$\langle f \rangle$	time averaged value
f''	subgrid quantity
f''	temporal standard deviation
g	convolution kernel
g_3	gravitational acceleration
h_i	subgrid heat flux
h	dipole height
k	wave number
p	pressure
q'	heat flux per unit length
q'''	heat flux per unit volume
r	radius
t	time
u_i	velocity component
x_i	spatial coordinate
C	model parameter
C_k	Kolmogorov constant
F_2	structure function
H	domain height
K_h	eddy diffusivity
K_m	eddy viscosity
$\mathscr{L}_{ij}$	test window stress
M_{ij}	dynamic scaling tensor
Pr	Prandtl number
Pr_t	turbulent Prandtl number
Ra	Rayleigh number
S_{ij}	rate of deformation tensor
T	temperature

Greek symbols

β	expansion coefficient
δ_{ij}	Kronecker delta
η	similarity coordinate
ϕ	similarity temperature
κ	thermal diffusivity
λ	thermal conductivity
ν	kinematic viscosity
τ_{ij}	subgrid stress
σ	radius
ω	vorticity
Δ	difference, grid-size
Ω	domain

laminar plume in unbounded space has been investigated numerically by Pera and Gebhart [17], where also supporting results of experiments are given. More extended experiments have been performed by Bill and Gebhart [3] who examined the transition to turbulence in detail. The behavior of turbulent plane plumes is reported by the experimental study of Rouse [19]. An integral (similarity) model based on an entrainment hypothesis as described by Turner [20] has been discussed by Bastiaans [1]. Most of the results mentioned above are collected in [7]. In this work also the influence of a partially confined space on the plume development is given, displaying the attracting influence of a side wall on laminar plumes.

In an entirely confined enclosure not much information is available on transitional plane plumes. From an engineering point of view, this flow is, however, very interesting. It is for instance related to the thermal conditions in boilers where it determines the efficiency of heat storage and to flow conditions inside electronic components where it determines durability of the equipment. The complexity of this flow might be due to the presence of sensitively interacting flow features resulting in strong intermittency. The latter flow characteristic is also connected to a low frequency meandering motion of the entire flow structure which is observed in this flow. Because of these phenomena it is difficult to obtain accurate statistics from experiments.

From a theoretical point of view it is difficult to identify features that are generic for all kinds of situations. Due to the confinement, a general analytical approach is of very limited relevance. Despite the complexity, practical problems as mentioned above, require information about this flow and on the influence of the confined geometry. Therefore, the numerical simulation is the only remaining method to study this flow.

Numerical simulation has only recently been applied to this type of flow. Results obtained with a 2D Direct Numerical Simulation (DNS) have been reported by Desrayaud and Lauriat [5] and Minev et al. [14]. These studies show transition phenomena such as Hopf and pitchfork bifurcations at low heat input as well as quasi-periodic and chaotic regimes. The pitchfork bifurcation is connected to symmetry breaking caused by the attraction of the lateral walls. Results obtained with 3D DNS have not been reported in the literature. In the present investigation, both, a 2D and 3D DNS will be considered of a transitional, buoyant plane plume above a line heat source in an enclosure. The objective is to study the characteristics and two-dimen-

sionality of this flow by comparison of the 2D and 3D results.

For a 3D DNS, a large computer capacity is needed, and even a single flow simulation requires considerable computational effort. In many engineering applications, parametric studies of this flow are needed and these require other computational techniques than DNS. In this case, the use of a LES is an attractive alternative because this technique requires much less computer time. However, in contrast with DNS, the LES method requires some modeling which is needed to represent the unresolved or sub-grid flow scales.

Most examples of these so-called sub-grid models in LES as documented in the literature, are concerned with shear flows. In many cases, the classical Smagorinsky model, as for instance described in [11], performs fairly well here. Successful examples of the application of the Smagorinsky model to fully turbulent channel flow are given by Deardorff [4] and Moin and Kim [15] as performed on a relative coarse and fine computational mesh, respectively. In the neighbourhood of solid walls there are however some deficiencies in most sub-grid models. Close to a wall there is a transition region where the flow changes from laminar to turbulent. This may perhaps be generalized to the present case, where we have a transitional flow, i.e. transition from laminar to turbulence and this may lead us to expect difficulties with the sub-grid modeling.

Capturing of a spatial transition by means of LES is not trivial. It has been proposed that a solution can be made to adapt the model constants to the local behavior of the flow in a dynamic way. This has been pioneered in [9] by the so-called ''dynamic model''. In thermal convective flows, an extra complication is provided by the interaction of the velocity and temperature field and the accompanying coupling of the closure assumptions for both processes. A standard way of treating the coupling is the application of a turbulent Prandtl number, though its value is not well established. Dynamic versions of the coupling are given in [12], revised in [1,23], but as will be shown, these cannot be applied directly in the case of spatially transitional plumes.

The sub-grid scale modeling in the case of a confined transitional plume has been studied experimentally in [2] by performing an a priori test. It is shown that, there is not only inter-scale kinetic energy transfer from large to small scales, but that the opposite transfer, i.e. ''backscatter'', is of equal importance in the transitional region. Furthermore, it is shown that the dynamic model is a good potential candidate for displaying the correct inter-scale kinetic energy transfer.

Before the results of a LES for the present flow can be trusted, the consequences of this sub-grid modeling have to be surveyed also in an a posteriori sense. Therefore, we aim to perform also a LES for the same flow as for which DNS is carried out. The results are then used to assess the influence of several sub-grid models used in the LES.

To give an outline of the paper, we first describe the numerical method for the DNS followed by a description of the SGS models for the large-eddy simulations. Then the problem that we consider here is defined. Subsequently, results are given, first, obtained with the 2D DNS followed by those with the 3D DNS. In the final part, the results of the LES computations obtained with various sub-grid models are discussed. The paper ends with a summary of the major conclusions.

2. Numerical approach and tests

2.1. Mathematical description and numerical method for DNS

The conservation equations for mass, momentum and energy formulated in terms of the Boussinesq approximation for the effect of buoyancy are

$$\frac{\partial u_i}{\partial x_i} = 0;$$

$$\frac{\partial u_i}{\partial t} + \frac{\partial}{\partial x_j}(u_i u_j) = -\frac{\partial p}{\partial x_i} + Pr\frac{\partial^2 u_i}{\partial x_j^2} + RaPr\Delta T\delta_{i3};$$

$$\frac{\partial T}{\partial t} + \frac{\partial}{\partial x_j}(u_j T) = \frac{\partial^2 T}{\partial x_j^2} + q''', \tag{1}$$

where the thermal diffusivity κ and the height of the flow domain, H, have been used as characteristic parameters to render these equations in their non-dimensional form. The Boussinesq hypothesis assumes the existence of a reference temperature and ΔT denotes the deviation from this reference temperature.

In the set of governing Eq. (1) two dimensionless quantities Ra and Pr appear. The first is the Rayleigh number Ra defined as

$$Ra = \frac{g_3\beta q' H^3}{\lambda\nu\kappa} \tag{2}$$

with q' the heat flux per unit length of the prismatic volume source

$$q' = \int_A q''' \, \mathrm{d}A.$$

and β the coefficient of thermal expansion taken at the reference temperature. The second dimensionless parameter is the Prandtl number given by

$$Pr = \frac{\nu}{\kappa} \tag{3}$$

where ν is kinematic viscosity. All fluid properties are assumed to be constant and equal to their value taken at the reference temperature.

The set of Eq. (1) has been solved numerically with help of a finite volume method adopted from Nieuwstadt (1990). Here, a short summary of the main characteristics of the method is given, and for more detail we refer to [1]. The spatial discretization is performed on a staggered grid with central differences for the diffusion terms and with the scheme of Piacsek and Williams [18] for the non-linear advection term. For the time integration, a leap-frog discretization is used except for diffusion for which, for stability reasons an Euler explicit forward in-time scheme is taken. To enforce continuity, the pressure correction method is used. For the advection of thermal energy, the second order upwind scheme of van Leer [22] is employed together with the "ULTIMATE" strategy of Leonard [10]. A weak time-filter is applied to prevent the solution from time splitting. To insure stability of the temporal integration, the time-step is restricted based on a criterion for the advection and diffusion of momentum and thermal energy. For relative large forcing of the flow, the numerical scheme is second-order accurate in space and time. Employing this method with sufficient resolution in time and space results in a direct numerical simulation.

2.2. Large-eddy simulations

The LES technique aims to simulate turbulent flows on a coarse grid. The basis of large-eddy simulation consists of the application of a spatial convolution filter to the governing equations. This procedure splits a generic turbulent variable f into a large scale component $\bar{f}$, and a sub-grid component f'. The decomposition and the convolution of f with a filter function g over the flow domain Ω are given by

$$f(x_i, t) = \bar{f}(x_i, t) + f'(x_i, t), \tag{4}$$

with

$$\bar{f}(x_i, t) = \int_{\Omega} g(x_i - x_i') f(x_i', t)\, \mathrm{d}x_i'. \tag{5}$$

and where the filter function g should satisfy the normalization condition

$$\int_{\Omega} g(x_i - x_i')\, \mathrm{d}x_i' = 1.$$

Application of the filter to the governing equations yields a description of the large scale motion according to

$$\frac{\partial \bar{u}_i}{\partial x_i} = 0;$$

$$\frac{\partial \bar{u}_i}{\partial t} + \frac{\partial}{\partial x_j}(\bar{u}_i \bar{u}_j) = -\frac{\partial \bar{p}}{\partial x_i} + Pr \frac{\partial^2 \bar{u}_i}{\partial x_j^2} + RaPr\overline{\Delta T}\delta_{i3} - \frac{\partial \tau_{ij}}{\partial x_j}$$

$$\frac{\partial \bar{T}}{\partial t} + \frac{\partial}{\partial x_j}(\bar{u}_j \bar{T}) = \frac{\partial^2 \bar{T}}{\partial x_j^2} + \bar{q}''' - \frac{\partial h_j}{\partial x_j}. \tag{6}$$

Application of the filter results in an unresolved flow field. Interactions in which unresolved flow scales participate, may influence the flow field at the grid-scale. Therefore, a Sub-Grid Model (SGM) is introduced, accounting for these influences. A LES requires an SGM that parameterizes the sub-grid stresses and sub-grid heat fluxes adequately, so that, the large flow scale can be accurately computed. Simulations with such a model are able to produce physically significant results at a relatively low computational effort.

The sub-grid stresses and fluxes which appear in Eq. (6), describe the interaction between the resolved and small scale field and are defined by

$$\tau_{ij} = \overline{u_i u_j} - \bar{u}_i \bar{u}_j \quad \text{and} \quad h_j = \overline{u_j T} - \bar{u}_j \bar{T}, \tag{7}$$

in the equation for the momentum and heat transport, respectively. The most common SGM is based on a gradient diffusion concept and is given by

$$\tau_{ij} = -2K_{\mathrm{m}} \bar{S}_{ij}, \quad \text{and} \quad h_j = -K_{\mathrm{h}} \frac{\partial \bar{T}}{\partial x_j}, \tag{8}$$

where the ratio of the sub-grid eddy viscosity K_{m} and the sub-grid eddy diffusivity K_{h} is defined as

$$Pr_{\mathrm{t}} = \frac{K_{\mathrm{m}}}{K_{\mathrm{h}}}. \tag{9}$$

When the turbulent Prandtl number Pr_{t} is given, only the eddy viscosity has to be parameterized in terms of resolved quantities. However, the value of Pr_{t} which typically lies in the range $\frac{1}{3} < Pr_{\mathrm{t}} < \frac{1}{2}$ (see [6]), is not well established.

In the present paper, we consider several sub-grid models. The first is the classical Smagorinsky model given by

$$K_{\mathrm{m}} = C\Delta^2 |\bar{S}|, \tag{10}$$

where the constant C can be estimated to be consistent with a Kolmogorov spectrum following [11] by

$$C = \pi^{-2} \left(\frac{2}{3C_{\mathrm{k}}} \right)^{3/2}, \tag{11}$$

with C_{k} the Kolmogorov constant.

As second SGM, we take the dynamic model proposed by Germano et al. [9]. In this model, the value of C is determined dynamically, depending on the local instantaneous flow behavior. In the formulation of [12], the equation from which C is obtained, reads

$$C = \frac{1}{2}\frac{\mathscr{L}_{ij}M_{ij}}{M_{kl}M_{kl}}, \tag{12}$$

in which the $\mathscr{L}_{ij}$ and M_{ij} are defined by

$$\mathscr{L}_{ij} = \widehat{\bar{u}_i\bar{u}_j} - \hat{\bar{u}}_i\hat{\bar{u}}_j \quad \textit{and} \qquad M_{ij} = \Delta^2\widehat{|\bar{S}|\bar{S}_{ij}} - \hat{\Delta}^2\big|\hat{\bar{S}}\big|\hat{\bar{S}}_{ij}, \tag{13}$$

respectively. The hat operator $\hat{}$ denotes a low-pass filtering with a kernel of size $\hat{\Delta} = 2\Delta$.

The third sub-grid model has been proposed by Métais and Lesieur [13] as

$$K_{\mathrm{m}} = 0.105C_{\mathrm{k}}^{-3/2}\Delta\sqrt{\bar{F}_2}, \tag{14}$$

with a filtered structure function

$$\bar{F}_2(\vec{x}) = \left\langle \left\| \vec{\bar{u}}(\vec{x}+\vec{r}) - \vec{\bar{u}}(\vec{x}) \right\|^2 \right\rangle_{\|\vec{r}\|=\Delta}, \tag{15}$$

in which the angular brackets indicate an ensemble averaging over the six neighboring grid-points. This SGM is known as the structure function model.

The fourth SGM to be used in our assessment is a Kolmogorov–Prandtl model given by

$$K_{\mathrm{m}} = C_\mu\Delta\sqrt{e_{\mathrm{sgs}}}; \quad C_\mu = \frac{1}{\pi}\left(\frac{2}{3C_{\mathrm{k}}}\right)^{3/2} \quad \text{and} \qquad C_{\mathrm{d}} = \pi\left(\frac{2}{3C_{\mathrm{k}}}\right)^{3/2}. \tag{16}$$

where e_{sgs} is sub-grid kinetic energy. This model requires an additional equation for e_{sgs} given by

$$\frac{\partial e_{\mathrm{sgs}}}{\partial t} + \frac{\partial}{\partial x_j}\left(\bar{u}_j e_{\mathrm{sgs}}\right) = 2K_{\mathrm{m}}\bar{S}_{ij}\bar{S}_{ij} - \frac{Ra\,Pr\,K_{\mathrm{m}}}{Pr_{\mathrm{t}}}\frac{\partial\bar{T}}{\partial x_i}\delta_{i3} + \frac{\partial}{\partial x_j}(K_{\mathrm{m}} + Pr)\frac{\partial e_{\mathrm{sgs}}}{\partial x_j} - C_{\mathrm{d}}\frac{e_{\mathrm{sgs}}^{3/2}}{\Delta}. \tag{17}$$

As a fifth and final sub-grid model, we use a buoyant Smagorinsky model which follows from balancing production and dissipation in Eq. (17), and which results in

$$K_{\mathrm{m}} = \sqrt{\frac{C_\mu^3}{C_{\mathrm{d}}}}\Delta^2\sqrt{2\bar{S}_{ij}\bar{S}_{ij} - \frac{Ra\,Pr}{Pr_{\mathrm{t}}}\frac{\partial\bar{T}}{\partial x_i}\delta_{i3}}. \tag{18}$$

This model accounts for turbulent diffusion in an unstable thermal stratification. In cases of local stable thermal stratification, the model is truncated as proposed by Eidson [6], where K_{m} is set to zero when the stratification term exceeds a positive gradient equal to the positive definite strain term. Besides the case of the dynamic procedure, the models contain only constants that are related to the Kolmogorov constant C_{k} and they are evaluated with help of the assumption $C_{\mathrm{k}} = 1.5$.

2.3. Two-dimensional plumes at Ra_{c}

The numerical code described in the previous section has been tested by comparison of its solution with results obtained by Desrayaud and Lauriat [5] for steady and unsteady confined buoyant 2D plumes. In a 2D rectangular enclosure, a plume is generated by a discrete point source. The no-slip boundary condition is satisfied on the walls of the domain. With respect to the thermal boundary conditions, the top and bottom wall are taken to be isothermal, whereas the lateral walls are adiabatic.

The source term in the energy equation in this case is given by

$$q''' = \delta(x - x_{\mathrm{s}})\delta(z - z_{\mathrm{s}}), \tag{19}$$

where δ is the Dirac delta function and $(x_{\mathrm{s}}, z_{\mathrm{s}})$ is the source position which is located at the position $(\frac{1}{2}, \frac{1}{4})$ in the computational domain, which itself has the dimension $\Omega = (0, 1) \times (0, 1)$ (the second direction is the z direction that corresponds to the index 3 in Eq. (6)). The Dirac function is approximated in the numerical representation by one grid volume with the condition that the integral across this grid volume equals unity. The Prandtl number is taken to be $Pr = 0.71$.

In their study, Desrayaud and Lauriat [5] have solved the non-dimensional form of the governing equations for the 2D case in vorticity–stream function formulation. For Rayleigh numbers lower than $Ra = 3.0 \times 10^7$, they find that the system is stable, i.e. it is attracted to a fixed point in phase space. At slightly higher Ra numbers, a purely periodic motion is observed after the flow has undergone a supercritical Hopf bifurcation. The critical value of Ra has been determined by linear extrapolation of the amplitudes at supercritical Ra numbers to a zero oscillation. With this procedure the critical Rayleigh number, Ra_{c} as found by Desrayaud and Lauriat [5], is close to $Ra = 3.0 \times 10^7$.

The numerical finite volume scheme utilized in the

present study was tested just below and above the bifurcation point. The results of this test are presented in [1]. Because of the lack of an exact reference also a spectral element method, as adopted from [14] was involved in the test. Employing these two methods very similar results are found compared to the results of [5]. Differences in any considered variable do not exceed a few percents, both in the stationary case and in the unsteady cases. With the finite volume method we have carried out a grid refinement study which indicates that the bifurcation point is somewhat lower than $Ra_c = 3.0 \times 10^7$. The present estimation is $Ra_c \simeq 2.8 \times 10^7$. This is supported by calculations of the same flow with the spectral element method mentioned above. Nevertheless, we are confident that with the finite volume method a fair accuracy is obtained at moderate grid resolution.

In the following sections we consider the simulation of a plume at $Ra = 10^{10}$ with help of the finite volume model discussed above. Again the confined plume is generated by a line source. All computations have been carried out for air, i.e. $Pr = 0.71$.

3. DNS of two-dimensional plumes at $Ra = 10^{10}$

3.1. Resolution requirements for the initial dipole

Different from the heat source definition in the previous section we proceed here first with a smooth and grid-independent description of the heat source. It is prescribed by a Gaussian hill with radius $\sigma = 2.5 \times 10^{-2}$ which is located at $(x_s, z_s)=(\frac{1}{2}, \frac{1}{4})$,

$$q''' = \frac{1}{\pi\sigma^2} e^{-r^2/\sigma^2}; \qquad r = \sqrt{(x - x_s)^2 + (z - z_s)^2}. \tag{20}$$

With grid resolutions starting at 45×45, this distribution can be represented with sufficient accuracy, i.e. the discrete integral of the heat flux over the domain does not differ more than 10^{-5} of the value 1. All calculations are performed at $Ra = 10^{10}$.

Let us first investigate the starting flow. As soon as the heat source is turned on, a warm dipolar vortex structure develops, which grows while rising to the top of the domain. A definition of the dipole height is given by

$$h = \frac{\int_\Omega \omega^2 (z - z_s)\, d\Omega}{\int_\Omega \omega^2\, d\Omega}$$

and this height is plotted as function of time in Fig. 1 for various grid resolutions (49^2, 99^2, 195^2 and 390^2). In addition, we show in Fig. 1, the resulting temperature field at time $t = 3 \times 10^{-4}$ at the finest resolution. At this moment in time, the dipolar structure at the plume front is fully developed. It has risen to

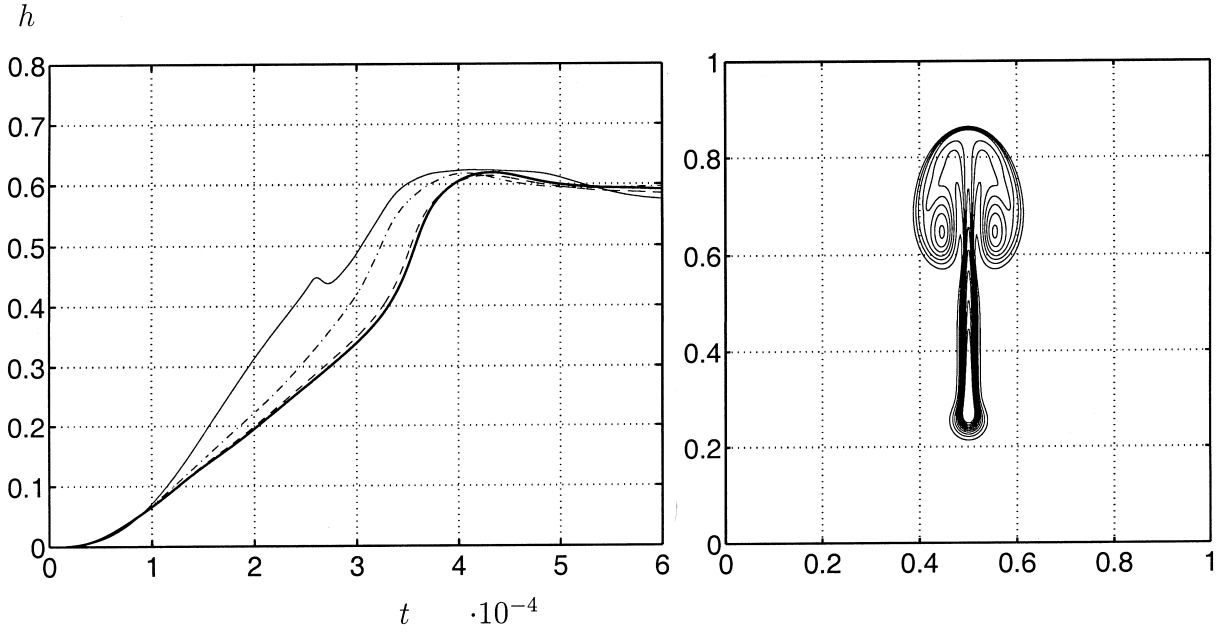

Fig. 1. Left: dipole height h as function of time for grid resolutions, 49^2: full thin line; 99^2: dash-dotted; 195^2: dashed; 390^2: full thick line. Right: temperature distribution at $t = 3 \times 10^{-4}$ at resolution 390^2, $Ra = 10^{10}$, $Pr = 0.71$. Contour levels [10^{-3}:10^{-3}:10^{-2}].

the upper half of the domain and is heading for the top wall of the confinement.

Results for various grid resolutions as given in Fig. 1 show that the dipole travels slower as the spatial resolution is increased. The reason for this is that, at low resolution the simulation is not able to capture the sharp velocity gradients with sufficient accuracy. In particular, this results in an underestimation of viscous friction and in a relatively large rising speed. At low resolution the spectral energy at wave-numbers connected to the grid size is not low enough to resolve the flow and this results in a wiggly shape of the temperature contours. When the grid resolution increases, the position and smoothness of the dipolar structure clearly converges to an asymptote. An acceptable grid-independent representation is obtained at the 195^2 grid. Stability of the numerical scheme specifies the allowable time-step in this case to be $\Delta t = 2.5 \times 10^{-7}$.

When time proceeds, the dipolar structure collides with the top wall. After this collision, the dipole splits into two mono-pole vortices which rebound from the no-slip wall. This rebound is accompanied by the creation of vorticity of opposite sign so that two new dipole structures are formed. A similar behavior has been also found experimentally by van Heijst and Flór [21] and numerically by Orlandi [16]. The two new dipoles penetrate into the more or less stagnant medium at the sides of the confinement. This drives a large scale recirculating flow in the upper part of the domain at both sides of the plume. After some time this large scale flow becomes unstable resulting in a meandering motion of the plume.

3.2. Laminar boundary layer flow

As an additional check of our numerical method and of the required resolution we compare the results of the 2D simulation with those obtained from laminar theory. The boundary-layer equations and their similarity solutions for the laminar plume are given in Appendix A.

For this comparison, we take from our 2D simulation an instantaneous flow field at a time where a symmetrical laminar plume has developed in the initial phase of the flow. Since the laminar boundary-layer theory is based on some approximations, the comparison might also be regarded as a check for the validity of this theory as given in Appendix A. For the boundary-layer theory to be valid, the forcing rate should be neither too small in order to still be dominated by convection, nor too large because the flow should not become turbulent.

The results of the comparison between the boundary-layer theory and the data of the full Navier–Stokes simulation on a 2D 195^2 grid are shown in Fig. 2. The simulation pertains to time $t = 5 \times 10^{-4}$. In this figure, the similarity temperature ϕ, as defined in Eq. (A13), is calculated from the computed values of T. The similarity variable η is calculated from the discrete grid coordinates for lines of constant height.

For the heat source distribution we have taken the

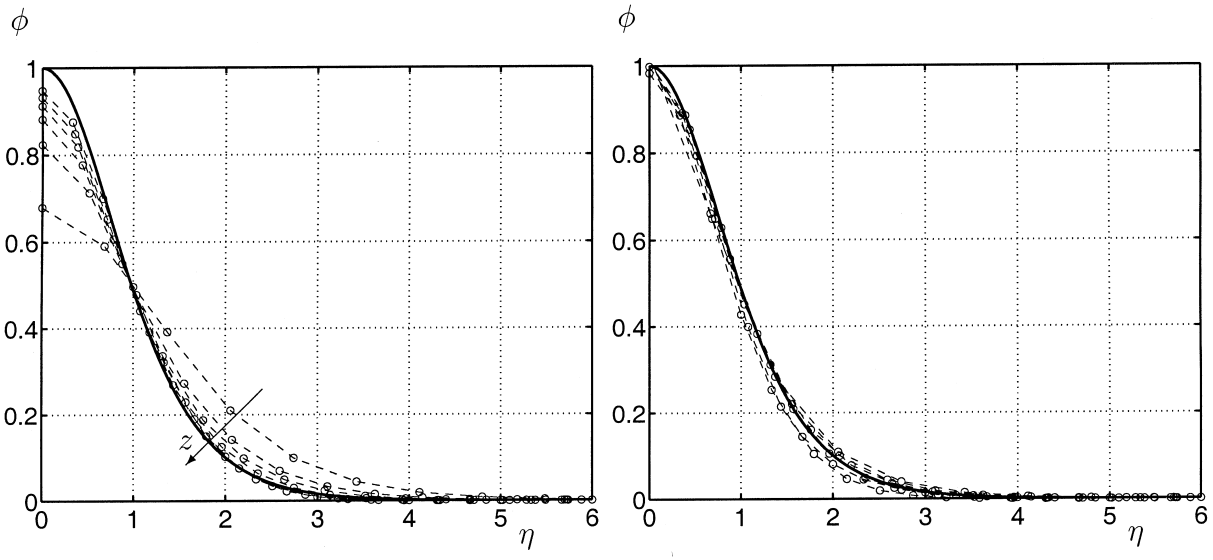

Fig. 2. Temperature distributions $\phi(\eta)$ at $t = 5 \times 10^{-4}$ and heights starting with $z = 0.3513$ to 0.9669 with $\Delta z = 0.1026$. Left: present Gaussian source. Right: point source containing a single grid cell. Circles indicate Navier–Stokes simulation grid points, the bold line indicates the boundary-layer theory result.

Gaussian hill given by Eq. (20) as well as a source contained in a single grid cell. It can be observed that the simulation with the latter source distribution matches almost exactly with the boundary-layer results. The small differences can be explained by the finite size of the heat source and the consequences of the confinement. In our calculation, the source distribution is finite and not equal to a point. This causes a decrease of temperature at small values of η, i.e. close to the heat source, compared to the result of the boundary layer approximation. The confinement is responsible for a recirculation which causes a small increase of the flow velocity along the source with an increased temperature. There is an increase of these effects in time because of the initial accumulation of recirculation and temperature. However, these effects are reduced by friction and cooling at the walls and also by diffusion.

For the Gaussian source we find larger deviations from the boundary-layer solution, especially at low heights where the source clearly can not be approximated by a point source. This results for low values of η in a temperature lower than the one obtained from the boundary-layer solution. At larger heights, the results are converging to the boundary-layer profile though they do not reach the value of $\phi = 1$ at the mid-plane. This is because, the height of the confinement is not large enough to reach a self-similar state. Temperatures at large η are larger than those obtained from boundary layer theory. This is a result of the broader heat source distribution and the recirculation. Additionally, the broader profile results in a smaller loss of heat of the fluid at the top wall so that more thermal energy is convected towards the plume region.

The conclusion is that, for the present confined geometry the laminar boundary-layer theory provides data that are in reasonable agreement with the simulated Navier–Stokes flow. This is the case for a time interval that starts with the collision of the initial dipole with the top wall and ends with the symmetry breaking instability after which the flow becomes turbulent. The time at which the flow becomes turbulent depends on the initial disturbances. For the phenomena occurring in the turbulent regime, the laminar boundary-layer results still provide good estimates of values for the characteristic velocities, temperatures and the boundary-layer thickness.

3.3. The predictability horizon in 2D flow

So far the analysis has covered only the instantaneously symmetrical flow field. The symmetry is a consequence of the geometry and of the boundary and initial conditions. The length of time period in which symmetric flow conditions persist, depends on the forcing of the flow and on the initial perturbations. In a numerical simulation this depends also on spatial resolution, temporal resolution and machine accuracy.

To investigate the time period after which non-stationary behavior sets in, we add temperature perturbations to the zero initial temperature field. With the help of an appropriate standard random generator, a sequence of random numbers is drawn for the temperature at each collocation point. The random numbers are distributed with a top-hat probability density in between the values $-a_T < T < a_T$, i.e. they are centred around zero so that no net thermal energy is added to the flow field. The intensity of the perturbation is varied in steps from $a_T = 10^{-14}$ to 10^{-4}. In each step the intensity is increased with two decades. The first value is close to machine accuracy as given by $\varepsilon \approx 10^{-15}$, for 64 bits floating point representations. The largest perturbations chosen are about one decade below the finally resulting temperature fluctuations.

The vertical velocity as function of time at a given point in the centre of the plume is illustrated in Fig. 3. The bold line is the result of the simulation with the smallest perturbation intensity, i.e. $a_T = 10^{-14}$. The initial peak which occurs at $t \sim 0.3 \times 10^{-3}$ corresponds to the passing of the dipole. After this initial behavior, the vertical velocity stays approximately constant until the onset of instability.

At the smallest perturbation intensity, the stationary behavior of the temperature is lost at approximately $t = 2.2 \times 10^{-3}$ and the symmetry of the flow is broken. At that moment a transverse motion of the plume occurs which results in a rapid decrease of the vertical velocity. From Fig. 3 it follows that with the increase of the perturbation intensity this transition occurs earlier. The largest perturbation disrupts the symmetry already immediately after the dipole collision with the top wall. The time required before the deviation from symmetry occurs, has been found to be insensitive to the exact distribution of the initial random perturbations. This is in contrast to the detailed solution which is determined by the exact initial conditions.

In the right frame of Fig. 3, we show the transition time as function of the initial perturbation intensity. Based on the assumption that an unstable linear mode is present, a fit is made of the data with an exponential function of time. Good agreement is found which suggests indeed a linear growth mechanism for initial perturbations. In terms of predictability we see that with every subsequent decade of accuracy of the approximation of the zero initial field, the predictability horizon is shifted forward in time with approximately the same time interval equal to 0.16×10^{-3}.

3.4. Turbulence statistics of 2D flow

The symmetry breaking bifurcation is the start of a

non-stationary flow eventually resulting in turbulence. Non-homogeneous turbulence develops in the plume above the buoyancy source. The turbulent structures that are generated, are convected by a recirculation. In the lower region of the domain these structures excite gravity waves of relatively low frequency. To investigate this 2D turbulent flow, statistics have been determined over the period $t = 0.005$–0.01. Again, we refer to the flow simulations at $Ra = 10^{10}$ and $Pr = 0.71$, and with a grid resolution of 195^2 equidistant volumes. In the temporal averaging it has not been assumed that the flow is symmetric which is suggested by the geometry and boundary conditions because the bifurcation may persist in the mean values. The resulting mean flow field is depicted in Fig. 4. Indeed, a large-scale flow bifurcation is present. The flow consists of a large asymmetric circulating region occupying most of the flow domain with a small oppositely circulating regions in the upper and lower left corner. According to the inverse energy cascade valid for 2D turbulence, energy injected at the source on small scales is transferred to large scales. This results in a large penetration of the recirculating flow in the initially stagnant lower part of the domain. Furthermore, part of the time the heat released at the source is being transported by the recirculating flow rather than moving under the influence of its own direct buoyancy. These effects can be observed in the instantaneous temperature plot shown in Fig. 4, in which there is a downward transport of the flow at the source position.

4. DNS of three-dimensional plumes at $Ra = 10^{10}$

The 3D DNS is carried out for $Ra = 10^{10}$ and $Pr = 0.71$ and consists of 37,000 time steps: the first 13,000 with size $\Delta t = 2.5 \times 10^{-7}$ and the last 24,000 with size $\Delta t = 2.0 \times 10^{-7}$. The period simulated with the longer time steps up to $t = 0.00325$ corresponds with the transient phase of the flow, whereas, the latter period up to $t = 0.00805$ deals with the quasi-stationary situation of the turbulent flow. A 3D random temperature perturbation with an intensity of $a_T = 10^{-8}$ has been added to the initial temperature field. The grid resolution is chosen to be 195^3, which is the same as for the 2D calculations. However, the grid independent convergence presented for 2D results is not a guarantee for the convergence in the 3D turbulent case, although we feel that it gives a good indication about the resolution required.

4.1. Transient flow results

The symmetry of the flow in the initial period found in the computation for two dimensions, occurs also in three dimensions. As soon as the symmetry breaking bifurcation appears, 3D effects become apparent. Although the start of the flow is 2D, the 3D simulation is used also for this period because this allows axial modes in the direction of the heat source direction, i.e. in y direction to grow right from the beginning.

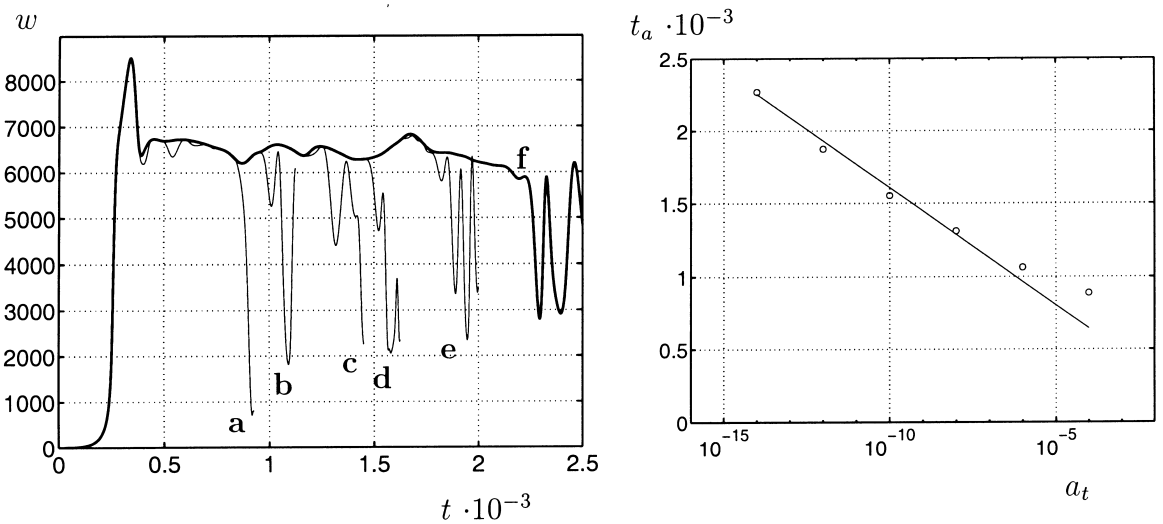

Fig. 3. Vertical velocity as function of time at position $(x, z) = (0.5, 0.7487)$. Left: influence of initial random perturbation on T with intensities $a_T = 10^{-4}$ (a), $a_T = 10 - 6$ (b), $a_T = 10^{-8}$ (c) $a_T = 20$ (c), 10^{-10} (d), 10^{-12} (e) and for the bold line $a_T = 10^{-14}$ (f). Right: time at which symmetry is lost t_a as function of the perturbation intensity. The full line represents the least squares fit for a logarithmic function: $t_a = -1.61 \times 10^{-4} \log(a_T)$.

The flow becomes asymmetrical at about $t = 0.00125$, which agrees with the 2D situation, depicted in Fig. 3. The transition to 3D motion occurs at $t \sim 0.0017$ as shown in Fig. 5. In this latter figure, the vertical and axial components of the velocity at a line along the y-axis at $(x, z) = (0.5, 0.75)$ are given as function of the axial coordinate y and time t. This monitoring line is located in transitional region, which is the region in which the temperature contours of the laminar plume are observed to break up. The values of the vertical and axial velocity components at the monitoring line are very sensitive to the transition. The growth and fluctuations of the axial velocity component at this location are caused by the transition, whereas small lateral oscillations have a large impact on the value of the vertical velocity, due to the small plume width. The mean value of the vertical component originates as a result of the potential to kinetic energy conversion. The fluctuating parts of both the vertical and axial velocity components appear as a result of downstream instabilities. Later on, velocity data at the monitoring line will be used as a key element in the comparison between DNS and LES.

The vertical velocity on the monitoring line shows that 3D motion initially manifests itself as a 2D flow with fluctuations along the axial y-direction. At the same time, axial velocity fluctuations appear. As the vertical velocity in the x–z planes get more out of phase at various values of y, the third velocity component in the y-direction starts to grow from its initial zero value. Note the difference in intensity scales for the vertical and axial velocity component. From the data presented, it can not be determined whether this velocity in the y-direction is due to a meandering of the laminar plume which is an asymmetrical solution or to a symmetrical solution with an axial change in profile height.

The instantaneous temperature field in the x–z plane is shown in Fig. 6 for the 2D and 3D computation. In the 2D case, large structures are present that bend and fold and which occupy almost the entire domain. As a result, the entire plume is found to oscillate heavily. In the 3D case, the plume exhibits a laminar structure at small heights above the source. At larger heights the plume becomes turbulent and smaller structures are created in agreement with 3D flow dynamics. Kinetic energy is in this case drained to smaller scales at which it develops no large recirculating flow. Therefore, the remaining recirculation, that is still present, is much less intense compared to the 2D case. Another difference of the 3D situation, connected to these differences in the dynamics, is that instantaneous temperature fields are more symmetric. Below the source, a region with a stable positive temperature gradient (also denoted as a thermocline) develops. Gravity waves in this thermocline are triggered by the unsteady motion in the upper part of the domain. This behavior contrasts with the 2D case where most of the time the lower region is penetrated by the large scale recirculations.

4.2. Flow statistics

The statistics of the flow were determined with help of of 24 instantaneous flow fields, equally spaced over the time interval $t = 0.00325$–0.00805 in which, quasi-

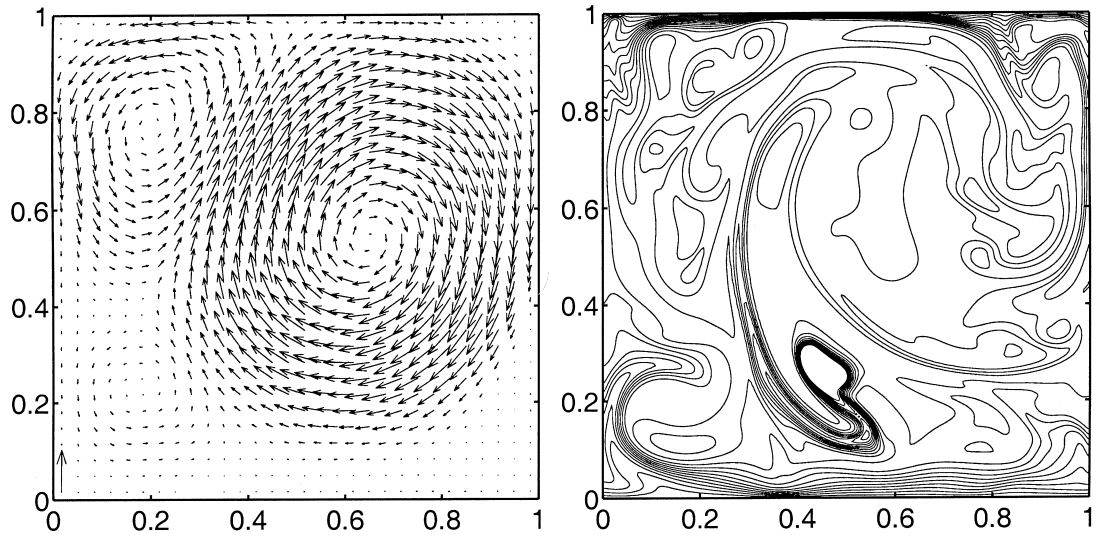

Fig. 4. Left: vector plot of time mean velocity at $Ra = 10^{10}, Pr = 0.71$. The lower left corner vector is of length 5000. Right: instantaneous temperature contours at $t = 0.0074$.

steady turbulence is present. Apart from averaging over these fields we have also performed an average over the homogeneous y-direction. A vector plot of the time mean flow is depicted in Fig. 7 from which it appears that the mean is characterized by convergence towards a flow which is symmetrical with respect to the mid-plane x_s.

As shown in Fig. 7, the time mean flow starts from the source position, splits in two parts at the ceiling and fills the upper part of the box with two recirculating regions. There is no mean penetration into the region below the source and a mean stagnant layer is present which we have denoted as the thermocline. Starting from the source there is a nearly linear spreading of the time mean flow field up to the vortex cores in the centre of the recirculation zones. Downstream of the entraining region, the flow collides with the top of the confinement and spreads to the upper left and right corner, following the wall without separation. Then, an almost vertical down-flow along the wall occurs, followed by a back-flow to the source position. Application of the entrainment assumption for plumes

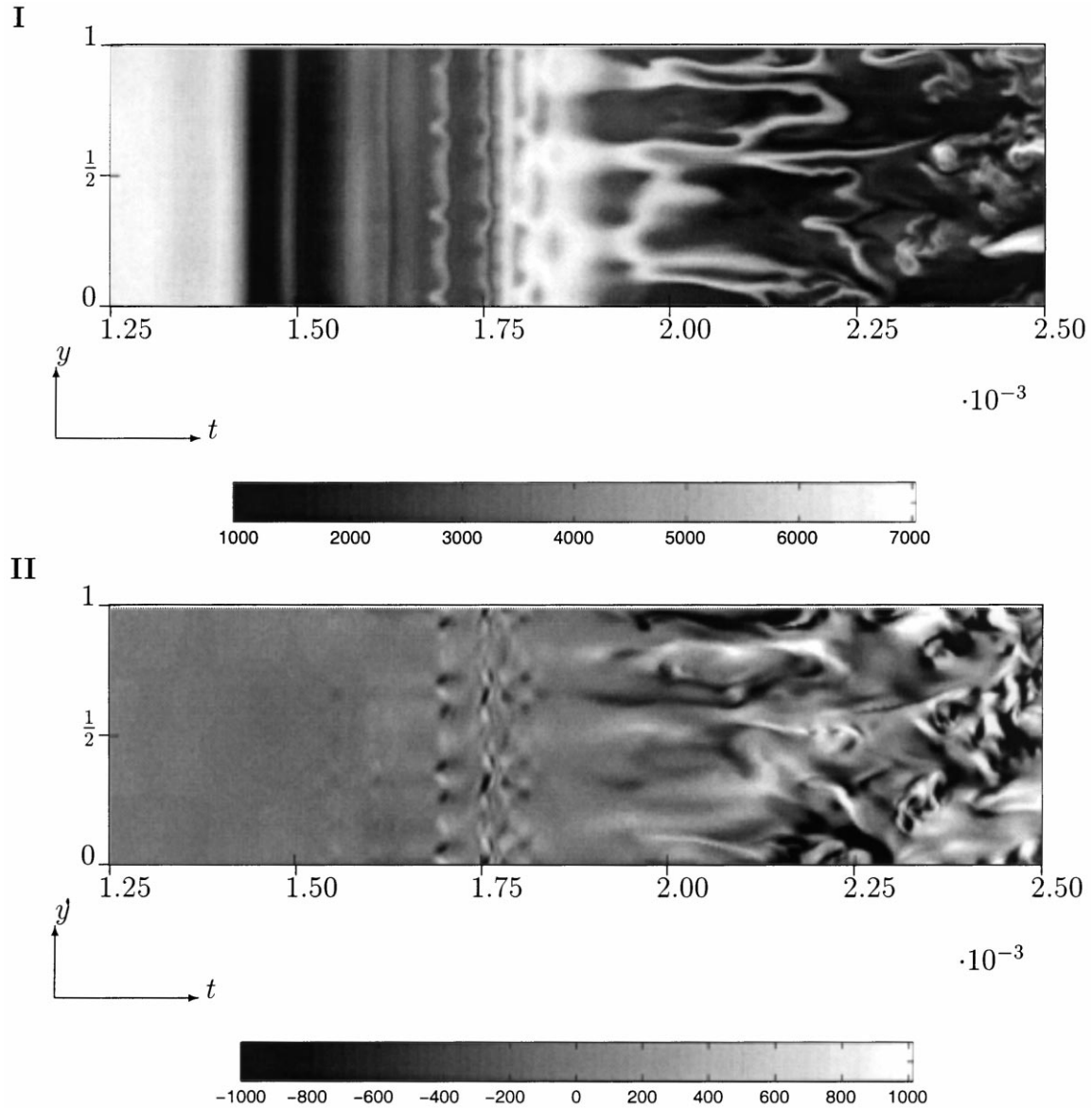

Fig. 5. Vertical velocity **I** and axial velocity **II** as function of axial coordinate and time at $x = 0.5$, $z = 0.75$. Evolution in simulated time interval $1.25 \times 10^{-3} < t < 2.5 \times 10^{-3}$, at $Ra = 10^{10}$, $Pr = 0.71$.

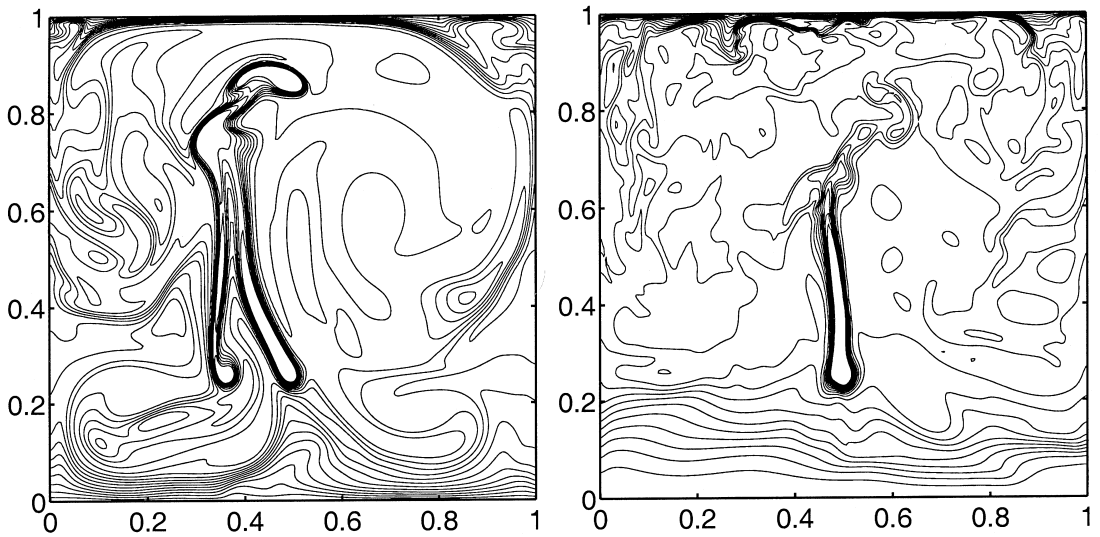

Fig. 6. Instantaneous temperature distributions at $Ra = 10^{10}$, $Pr = 0.71$, $t = 8.0 \times 10^{-3}$ in the 2D case (left) and 3D case (right). Contour values (0.0005:0.0005:0.01).

in unbounded space, as mentioned in the introduction and discussed in detail in [1], results in a self similar turbulent flow profile with a constant maximum time mean vertical centre-line velocity of nearly 2800. The value of this velocity component as found by the present DNS is not much larger than 2000. Thus, the bounded flow domain together with transitional flow phenomena alters the flow severely, compared to the free turbulent plume.

All velocity fluctuations for the 3D plume exhibit a maximum value in the centre of the box near the top wall which differs from the resulting velocity statistics for the 2D plume. This is shown in contour plots of these fluctuations illustrated in Figs. 8 and 9. Especially the standard deviation of the vertical and axial components show large values in the upper part of the domain. The latter exhibits a particularly large increase in a thin layer at the upper wall. From these figures and from the evolution of the temperature field shown

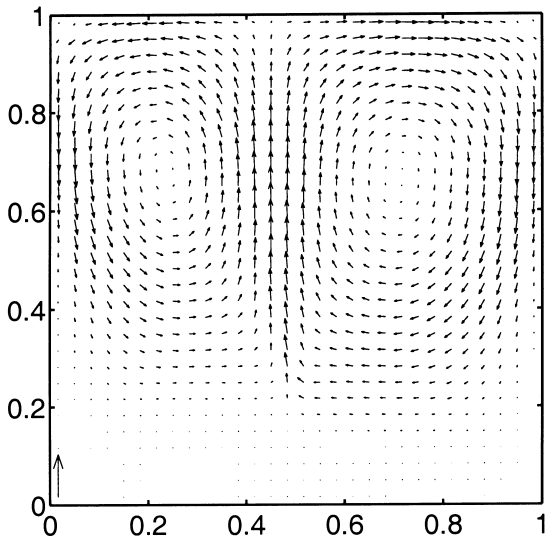

Fig. 7. Vector plot of time mean velocity at $Ra = 10^{10}$, $Pr = 0.71$. Lower left corner vector is of length 5000.

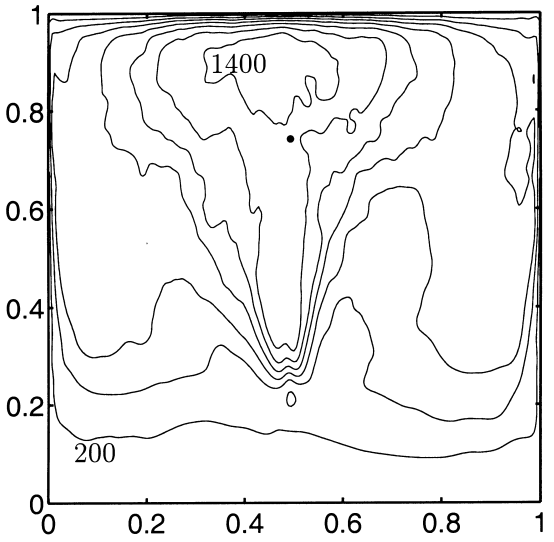

Fig. 8. Contour plot of the standard deviation of the vertical velocity w at $Ra = 10^{10}$, $Pr = 0.71$. Contours starting at 200 and increasing with 200. The dot denotes the monitoring line illustrated in Fig. 5.

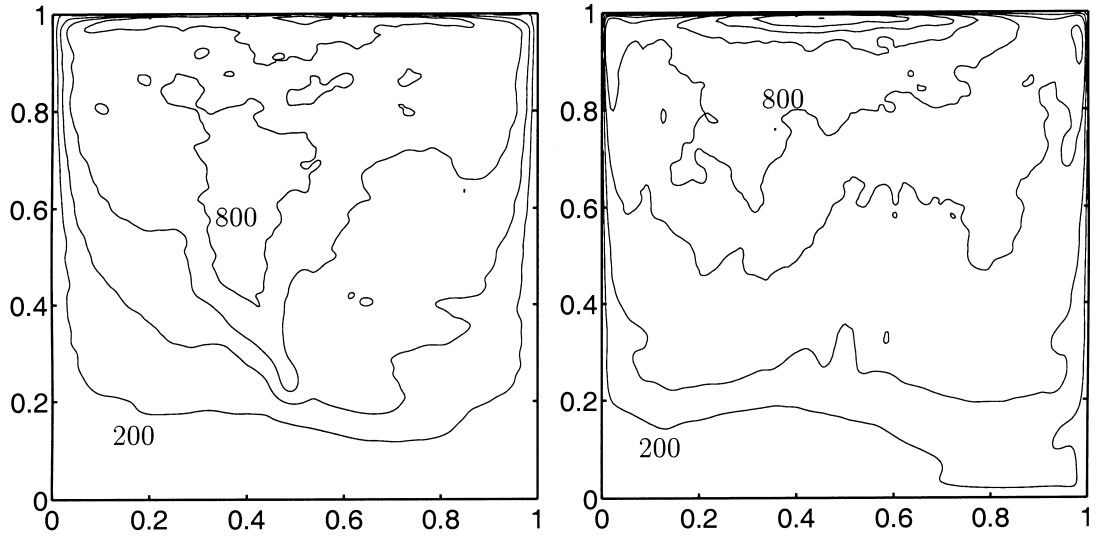

Fig. 9. Contour plot of the standard deviation of the horizontal velocity u (left) and axial velocity v (right) at $Ra = 10^{10}$, $Pr = 0.71$. Contours starting at 200 and increasing with 200.

in Fig. 5 it can be concluded that the flow is essentially three-dimensional.

From the axial velocity data recorded at the monitoring line $(x, z) = (0.5, 0.75)$, spectral and probability density distributions have been computed and these are given in Fig. 10. The frequency axis for the temporal spectrum is scaled with the mean vertical component of the velocity $\langle w \rangle$.

The spectrum decreases as function of the wave number with increasing rate at larger wave-numbers. This shape is the result of several simultaneously occurring phenomena. The first factor is the buoyant source that is defined to possess a relatively small spatial dimension. This source is responsible for the injection of kinetic energy into the modes of relatively high wave numbers in the x-direction. In the transi-

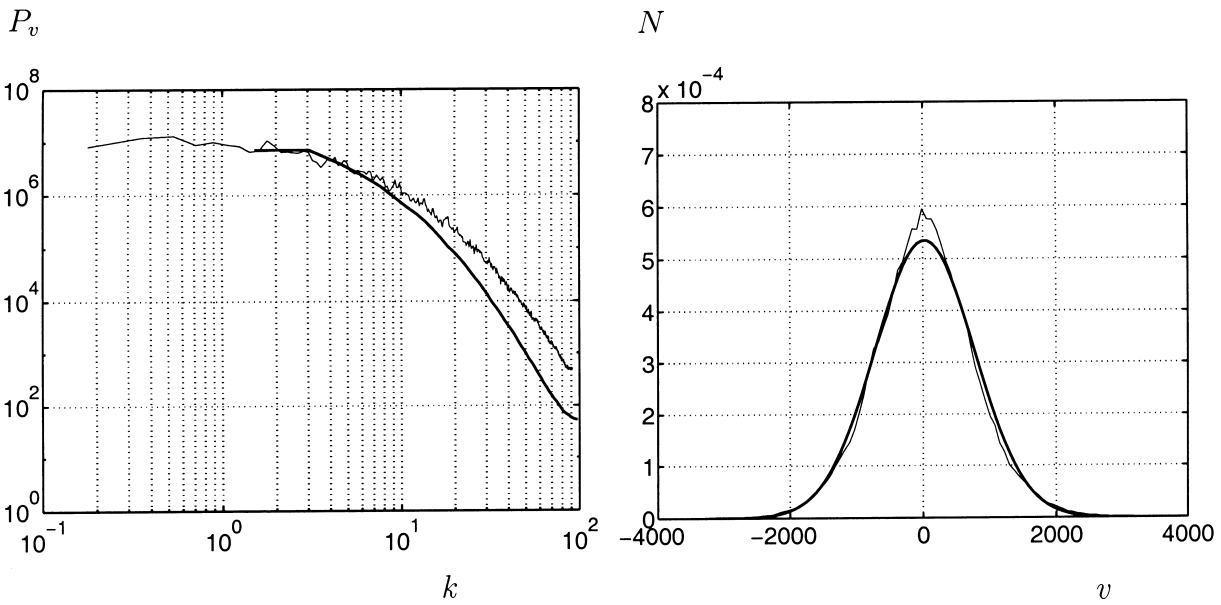

Fig. 10. Statistics of the axial velocity at the line $(x, z) = (0.5, 0.7487)$. Left: spectral density, bold line: spatial, thin line: temporal (frequencies divided by $\langle w \rangle$); right: normalized distribution, thin line: result from simulation, bold line: Gaussian with same mean and standard deviation.

tional region, the plume bends and folds and the kinetic energy is transferred to modes in the other two directions. This results, on an average, in structures that have a rising motion with an increased width and which are responsible for the large-scale recirculation as observed in the time mean flow. The large-scale recirculation on its turn interacts with the smaller scales provided by the laminar and transitional plume resulting into a gradual loss of large-scale kinetic energy to the smaller scales. During the transitional bending and folding process, there is a redistribution of kinetic energy, probably both up-scale and down-scale. There is no clear equilibrium range and the spectrum cannot be explained by any simplified assumptions. However, the influences of small scales on large scales might be small. In this case, LES might be an alternative to simulate the flow.

The temporal and spatial spectrum shown in Fig. 10 agree very well at low wave-numbers. At high frequencies a larger convection velocity is needed to obtain the same agreement. This implies that small scale structures have a relatively large convection speed. A physical interpretation of this phenomenon might be that small scale structures emerge from the laminar plume, which at the time is positioned in the mid-plane and is oriented in the vertical direction. Thus, the convection speed for small scale structures is large. After the initiation of small scales in this transitional region, these scales effect on their turn, the laminar plume by pushing it out of the centre-plane which results in a roll up of the laminar plume. This creates structures of a larger spatial extent, and the mean velocity at which they are convected, is diminished. This scenario repeats itself in an intermittent way. The probability density distribution shows an almost Gaussian shape.

5. LES of three-dimensional plumes at $Ra = 10^{10}$

Next, we consider the results obtained with a LES on relatively low resolution of 45^3 collocation points. The computations have been carried out for the same flow conditions as for which we have performed the DNS presented in the previous section. Computations have been performed with the sub-grid models discussed in the section concerning large-eddy simulation. All model constants used in the sub-grid models that need to be prescribed explicitly, are computed based on a Kolmogorov constant $C_k = 1.5$. The LES simulations consisted of 40,000 time steps of length $\Delta t = 5 \times 10^{-7}$. The last 20,000 time steps were used to calculate the statistics in the time interval $t = 0.01$–0.02.

Results obtained with the different sub-grid models for the mean values and standard deviations of the vertical and axial velocity components at the monitoring line $(x, z) = (0.5, 0.75)$ are listed in Table 1 together with the DNS data. In the table and in the following time mean quantities are denoted by angular brackets, whereas standard deviations are denoted by a double prime. To make a fair comparison between the LES and DNS results, a spatial filtering operation of the DNS is necessary. The LES is performed on a 45^3 grid, whereas, the grid is defined by 195^3 collocation points. The ratio of grid resolutions has thus a value of $4\frac{1}{3}$, which is not an integer. In order to obtain a lower bound estimate for the sub-grid fluctuations, a top-hat convolution filter of size 5Δ is applied on the DNS data. The filtering of the DNS data results in $\bar{w}'' = 1282$, and $\bar{v}'' = 727$, whereas, the results for full resolution are $\bar{w}'' = 1328$ and $\bar{v}'' = 746$, respectively. We note that the time mean components are not affected by this filtering operation.

In general it is observed that deviations of LES results with DNS data observed at the monitoring line, have the same tendency, i.e. in the same direction, over the entire domain. Thus, Table 1 gives a good qualitative impression of the performance of several sub-grid scale models. The time mean axial velocity component in Table 1 shows only slow convergence to zero. A small deviation is left which relative to the standard deviation lies typically within 3% and this is considered to be sufficient. The Rayleigh number is too

Table 1
Flow statistics at $(x, z) = (0.5, 0.7487)$ produced by DNS and several LESs

	$\langle\bar{w}\rangle$	$\bar{w}''$	$\langle\bar{v}\rangle$	$\bar{v}''$
DNS	1824	1282	22	727
Zero model	2353	1292	−10	761
Smagorinsky model	2069	1293	19	676
Smagorinsky model $Pr_t = 1/2$	1993	1302	10	682
Structure function model	1912	1353	65	703
Buoyant Smagorinsky model	2375	1255	−17	621
Kolmogorov–Prandtl model	2114	1274	13	699
Dynamic model	2324	1283	−25	775

low to expect isotropy but nevertheless, the fluctuations of the two velocity components do not differ very much. Furthermore, the intensity of the mean flow and the fluctuation are within the same order of magnitude, as expected in natural convection flows.

With respect to the mean flow, indicated by $\langle\bar{w}\rangle$, a better agreement is obtained with the more simple models, like the Smagorinsky model and particularly, the structure function model. With the latter model, the difference with the DNS lies within 5%. A further improvement is obtained if the turbulent Prandtl number is increased. The zero model (i.e. no sub-grid model or $\tau_{ij} = 0$) as well as the buoyant Smagorinsky model and the dynamic model result in an over-estimation of the mean flow, up to 30% for the buoyant Smagorinsky model. The dynamic model yields minimal and even negative values for the dynamic parameter C in the plume region. In keeping the numerics stable, a lower bound of zero had to be applied to the sub-grid constant. Thus backscatter, an important phenomenon in the plume region [12], is directly prohibited. This explains that the results of the dynamic model are similar to those of the $\tau_{ij} = 0$. The buoyant Smagorinsky model, on the other hand, yields an increased eddy viscosity due to the unstable local stratification within the plume and thus, to reduced fluctuations and subsequently to a large mean kinetic energy. By putting the stratification effect in a non-equilibrium description like the Kolmogorov–Prandtl model, an improvement is obtained with respect to the buoyant Smagorinsky model.

Except for the buoyant Smagorinsky model, the differences in the velocity fluctuations are not as large as for the mean velocity. In contrast with its excellent performance for the mean flow, the structure function model results in the largest deviation from the DNS data for the fluctuations of the vertical velocity with a value of about 5%. However, from the mean value of the axial velocity it follows that results may still be far away from the convergence. The fluctuations in axial velocity as obtained by the models differ with a maximum of 7%. This value is reached by the dynamic model in the form of an overestimation as caused by aliasing effects. This is the result of the fact that the diffusivity coefficients are very low causing high wave number modes to emerge. These wave numbers must be represented on the grid-scale by the numerical scheme because of its energy conserving property. On the other side, the same relative difference with an underestimation of fluctuations of axial velocity is obtained with the standard Smagorinsky model. The difference is made in allowing grid-scale fluctuations with the dynamic model and dissipating them rigorously with the Smagorinsky model.

The distribution of the statistical quantities over the x–z plane for all variables is found to be similar to the distribution computed from the DNS. Due to the longer integration time, a better convergence is obtained and the fields are more symmetrical than the DNS data. As an example, the time mean vector plot for the simulation with the Smagorinsky model at $Pr_t = 1/3$ is given in Fig. 11. A comparison of the structure of the mean flow with the DNS result of Fig. 7 shows a good agreement.

Next, we consider the spectra and distributions of the fluctuations as obtained by LES simulations and compare these with the DNS data. Again, for the assessment of DNS data with LES values, a filter operation should be performed on the DNS data before calculating distributions and spectra. However, since the distributions are more or less Gaussian, its shape for the filtered velocity is determined by the values in Table 1. With respect to the spectra, we find that up to the Nyquist wave number of the LES results, there is almost no difference of filtered DNS data compared to filtered DNS results. At this wave number, $k = 22.5$, the intensity decrease in the spectrum as a result of the filtering operation is only about 19%. Note that application of a top hat filter with a width $\Delta = 1/45$ in the Fourier domain, G, results in a spectrum multiplied with a factor equal to

$$G^2 = \left(\frac{\sin(\pi k\Delta/2)}{(\pi k\Delta/2)}\right)^2.$$

At higher wave numbers, the decrease rises to 100% at $k = 90$.

As a result of the longer integration time used in the

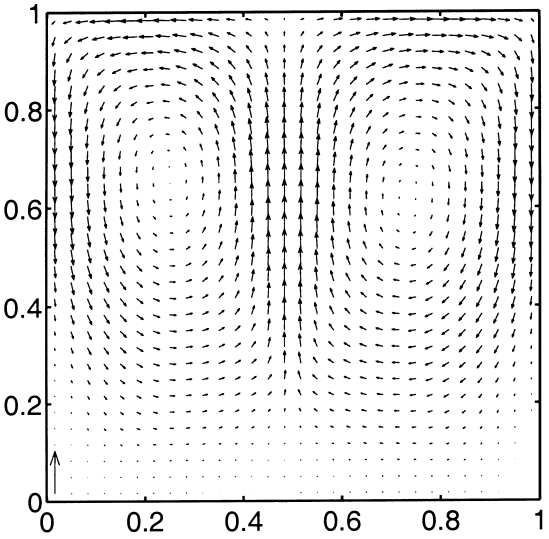

Fig. 11. Vector plot of time mean velocity at $Ra = 10^{10}$, $Pr = 0.71$, obtained with Smagorinsky model, $Pr_t = 1/3$. Lower left corner vector is of length 5000.

LES, the distribution of observed values of the axial velocity is closer to a Gaussian distribution compared to the DNS case. The resulting spectra computed from a time series collected at the monitoring line are given in Fig. 12 for the cases computed with the Smagorinsky and the dynamic model. At low wave-numbers, the spatial spectrum as obtained by both models show a decreased energy by a factor of about four compared to the DNS result of Fig. 10. This is in contrast to the temporal spectrum at low frequencies which shows an excellent agreement with the DNS data. This means that the axial velocity at the monitoring line fluctuates as a whole in time without the correct variations in the axial direction. Thus, the lower amount of fluctuations present in the spatial spectra compared to the temporal spectra and also the spatial spectrum of the DNS may be regarded as a return to a more 2D organized flow, which still describes a chaotical meandering motion. From this observation it may be concluded that, the laminar to turbulent transition of the plume is clearly affected by applying a LES with the mentioned subgrid models. At higher wave-numbers, the spatial spectrum as obtained by the Smagorinsky model decreases, similar to the DNS. Due to the decreased eddy viscosity as estimated by the dynamic model, its result shows relatively large intensities of the spatial small scale fluctuations. At the highest wave-number, the intensity of the axial velocity fluctuations of the dynamic model exceeds the intensity of the DNS.

At low frequencies the temporal spectrum of the axial velocity at the monitoring line as obtained by the les simulations agree very well with the dns data. The results obtained with the Smagorinsky model follows the spectrum of the DNS up to a wave-number of about four. At larger wave-numbers the spectrum gradually deviates more and more. The temporal spectrum of the dynamic model result shows an excellent coverage of the dns data up to a wave-number of 13 after which the les spectrum falls off quite rapidly.

6. Conclusions

Buoyant air flow above a line source of heat in a confined geometry has been investigated with help of DNS and LES. In order to study the required grid resolution, first 2D simulations have been performed. By investigating the grid independence it is found that for the 2D case at $Ra = 10^{10}$ and $Pr = 0.71$, a grid resolution of 195^2 grid points is sufficient to adequately simulate the flow. The 2D simulations are also used to study the behavior of the initial transient and the loss of stability. For the case of an initial steady flow, the laminar boundary layer solutions are found to match the present full 2D Navier–Stokes solutions very well.

The stability of the flow is studied by imposing perturbations on the initial temperature field. When the intensity of these perturbations is increased, stability is lost at an earlier stage. Based on these results, a suitable intensity has been found for the initiation of the 3D DNS, resulting in a relatively

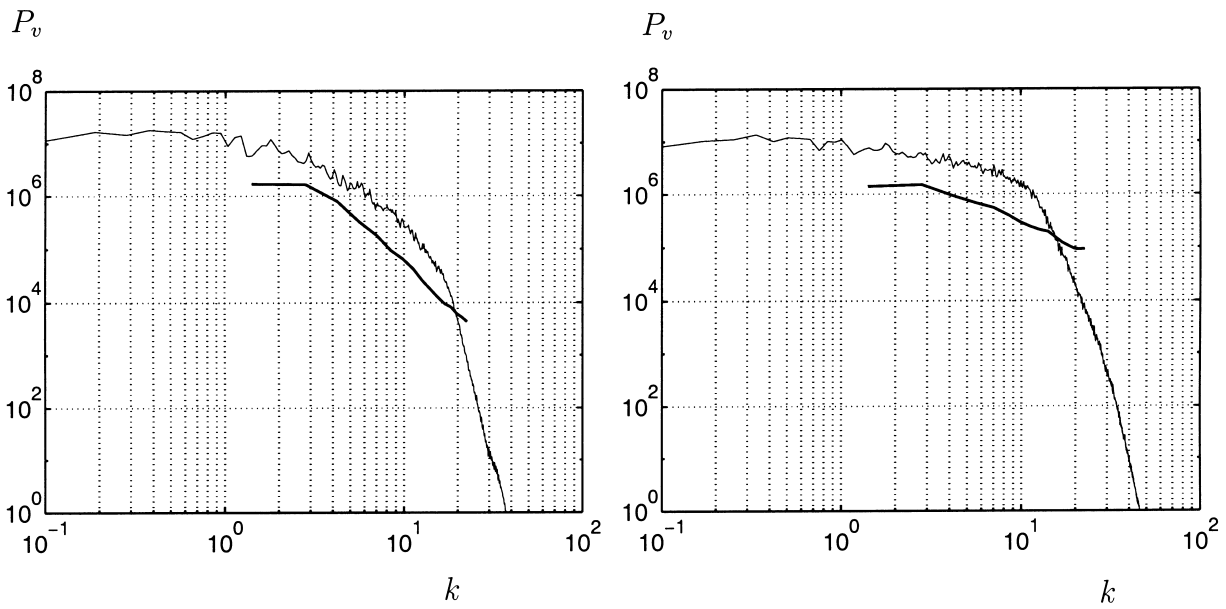

Fig. 12. Spectral densities of the axial velocity at the line $(x, z) = (0.5, 0.7487)$. Bold line: spatial, thin line: temporal (frequencies divided by $\langle w \rangle$). Left: result obtained with Smagorinsky model; right: results of dynamic model.

fast growing transient without too much disruption of the flow. Statistics of the 2D turbulent flow show a large-scale circulating pattern which is not symmetric. Large fluctuations on this background flow are convected by the mean circulation with a low dissipation rate.

The 3D DNS behaves in its initial phase as the 2D flow. After some time temporal and spatial fluctuations appear of the vertical velocity and the velocity in the direction of the line heat source, i.e. the axial direction. These are studied at the monitoring line positioned at $(x, z) = (0.5, 0.7487)$. Shortly after the symmetry breaking bifurcation, 3D structures appear in the flow. In this stage, the deviation of the axial velocity from its initial zero value is still negligible relative to fluctuations of the vertical velocity with the axial coordinate. From this stage on, these axial velocities started to grow up to their steady state statistics.

The time mean turbulent flow which emerges after the transient conditions described above, shows a symmetrical profile. It is found that all fluctuations have their maximum near the top wall in the centre of the box. Particularly the fluctuations in the axial direction show a relatively sharp increase just below the top wall. Spectra of the axial velocity component are found to fall off fast with increasing wave-numbers and frequencies.

Following the DNS we have performed LES computations with several sub-grid models are considered. On the average, most of these LES computations result in a solution which is similar to the DNS. Especially, the relatively simple equilibrium models lead to a good agreement between LES and DNS. The Smagorinsky model extended with a buoyant production term results in a strong deviation with the dns. Application of the Kolmogorov–Prandtl model, which is basically a similar approach, results in a better agreement.

In the use of these sub-grid models, tuning of the model constants seems to have the potential of yielding even better results. Therefore, dynamic modeling is considered to be advantageous. Yet, application of the dynamic procedure to the turbulent stresses did not result in a satisfactory performance. In the plume region, the dynamic parameter is estimated to be negative in a significant amount of time. In order to keep the numerics stable, a lower bound of zero had to be applied to the sub-grid constant. As a result backscatter, an important phenomenon in the plume region, is directly prohibited. This gives rise to results almost identically equal to the simulation with the $\tau_{ij} = 0$ model, i.e. the case of no sub-grid-model case.

The spatial spectra of the axial velocity of LES computations showed relatively small intensities compared to the DNS, whereas the temporal spectra displayed an excellent agreement. In the LES results at the monitoring line, the plume moves back and forth in the axial direction. This is the most striking difference between LES and the DNS showing a clear influence on the transitional region.

Acknowledgements

This work was sponsored by the Stichting Nationale Computerfaciliteiten (National Computing Facilities Foundation, NCF) for the use of supercomputer facilities, with financial support from the Nederlandse Organisatie voor Wetenschappelijk Onderzoek (Netherlands Organization for Scientific Research, NWO).

Appendix. Similarity solutions for the laminar boundary layer

Analogous to the description of Gebhart et al. [7], the governing non-dimensional continuity, momentum and energy equations are simplified by means of the boundary-layer assumptions to yield the following set of equations

$$\frac{\partial w}{\partial z} + \frac{\partial u}{\partial x} = 0; \tag{A1}$$

$$w\frac{\partial w}{\partial z} + u\frac{\partial w}{\partial x} = Ra\,Pr\,T + Pr\frac{\partial^2 w}{\partial x^2}; \tag{A2}$$

$$w\frac{\partial T}{\partial z} + u\frac{\partial T}{\partial x} = \frac{\partial^2 T}{\partial x^2}. \tag{A3}$$

These equations are solved by introducing a similarity variable $\eta(z, x)$ and a stream-function $\psi(z, x)$ (defined by $w = \partial\psi/\partial x$ and $u = -\partial\psi/\partial z$) and a temperature deviation, which are defined as follows:

$$\eta(z, x) = b(z)x;$$

$$\psi(z, x) = c(z)f(\eta);$$

$$T(z, x) - T_\infty = d(z)\phi(\eta). \tag{A4}$$

Here, f is the similarity stream-function and ϕ, the similarity temperature. Substitution in the boundary-layer equations leads to the following set of ordinary differential equations for f and ϕ

$$Pr\,f''' + \frac{c_z}{b}ff'' - \left(\frac{c}{b^2}b_z + \frac{c_z}{b}\right)f'^2 + RaPr\frac{d}{b^3 c}\phi = 0;$$

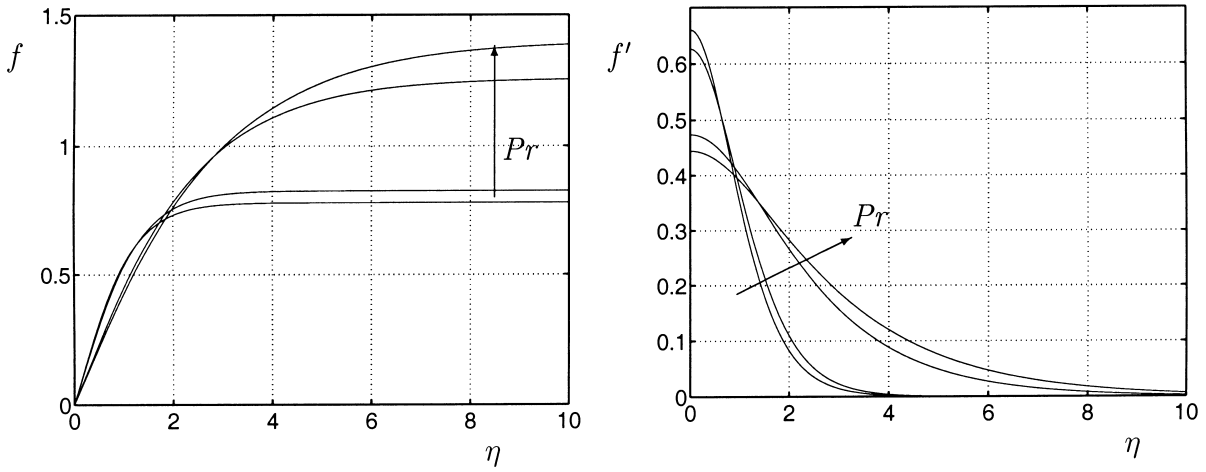

Fig. A1. Calculated similarity stream-function (left) and velocity (right) profile.

$$\phi'' - \frac{cd_z}{bd} f'\phi + \frac{c_z}{b} f\phi' = 0. \tag{A5}$$

The primes denote differentiation with respect to η and the subscript z denotes partial differentiation with respect to the vertical direction z.

The existence of a similarity solution now requires that the coefficients in this set of equations are not z-dependent which results in

$$b(z) = \frac{1}{z}\left(\frac{1}{4} Ra\ Pr\ d(z) z^3\right)^{1/4};$$

$$c(z) = 4b(z)z;$$

$$d(z) = Nz^n. \tag{A6}$$

Now the set of ordinary differential equations can be written as

$$Pr\, f''' + (n+3) f f'' - (2n+2) f'^2 + \phi = 0;$$

$$\phi'' - 4n f'\phi + (n+3) f\phi' = 0. \tag{A7}$$

An additional requirement is given by the fact that the buoyancy flux must be equal to the heat input. The latter was scaled to unity which leads to

$$\int_{-\infty}^{+\infty} w(T - T_\infty)\, \mathrm{d}x = 1. \tag{A8}$$

The buoyancy flux thus does not depend on z, and from this it follows, respectively, to

$$n = -\frac{3}{5}; \tag{A9}$$

$$N = (4^3 I^4 Ra\ Pr)^{-1/5} \tag{A10}$$

where the integral I has to be evaluated from the boundary-layer solution, according to

$$I = \int_{-\infty}^{+\infty} f'(\eta)\phi(\eta)\, \mathrm{d}\eta. \tag{A11}$$

Using appropriate boundary conditions, the boundary layer equations can now be integrated. These conditions are given by the symmetry around $x = 0$, the definition of ϕ, and the vanishing of w or T at $\eta \to \infty$ (since these are not independent), resulting in

$$f'(0) = f''(0) = f'(\infty) = \phi'(0) = \phi(0) - 1 = 0. \tag{A12}$$

By numerical integration, solutions can be obtained for $\phi(\eta)$, $f(\eta)$ and $f'(\eta)$ as function of Pr. The results

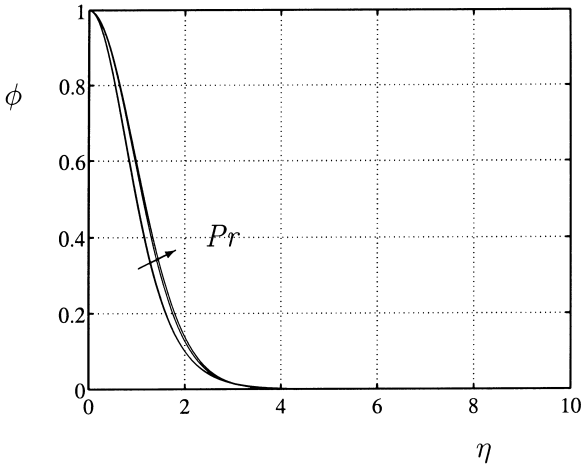

Fig. A2. Calculated similarity temperature profiles.

for these quantities are given in Figs. A1 and A2 for values of Pr equal to 0.71, 1.0, 5.0 and 7.0.

Now it is possible to calculate the relevant variables u, w and T with

$$u = \frac{2}{5}(2I^{-1}Ra\,Pr)^{2/5}xz^{-4/5}f'(\eta) - \frac{3}{5}(4^3I^{-1}Ra\,Pr)^{1/5}z^{-2/5}f(\eta);$$

$$w = (2I^{-1}Ra\,Pr)^{2/5}z^{1/5}f'(\eta);$$

$$T - T_\infty = (4^3I^4Ra\,Pr)^{-1/5}z^{-3/5}\phi(\eta). \quad \text{(A13)}$$

References

[1] R.J.M. Bastiaans, Large-eddy simulation of confined transitional plumes, PhD thesis, Eindhoven University of Technology, ISBN 90-386-0259-6, 1996.

[2] R.J.M. Bastiaans, C.C.M. Rindt, A.A. van Steenhoven, Experimental analysis of a confined transitional plume with respect to subgrid-scale modelling, Int. J. Heat Mass Transfer 41 (1998) 3989–4007.

[3] R.G. Bill Jr, B. Gebhart, The transition of plane plumes, Int. J. Heat Mass Transfer 18 (1975) 513–526.

[4] J.W. Deardorff, A numerical study of three-dimensional turbulent channel flow at large Reynolds numbers, J. Fluid Mech 41 (1970) 453–480.

[5] G. Desrayaud, G. Lauriat, Unsteady confined buoyant plumes, J. Fluid Mech 252 (1993) 617–646.

[6] T.M. Eidson, Numerical simulation of the turbulent Rayleigh–Bénard problem using subgrid modelling, J. Fluid Mech 158 (1985) 245–268.

[7] B. Gebhart, Y. Jaluria, R.L. Mahajan, B. Sammakia, Buoyancy Induced Flows and Transport, Hemisphere, Washington, DC, 1988.

[8] B. Gebhart, L. Pera, A.W. Schorr, Steady laminar natural convection plumes above a horizontal line heat source, Int. J. Heat Mass Transfer 13 (1970) 161–171.

[9] M. Germano, U. Piomelli, P. Moin, W.H. Cabot, A dynamical subgrid-scale eddy viscosity model, Phys. Fluids A 3 (7) (1991) 1760–1765.

[10] B.P. Leonard, The ULTIMATE conservative difference scheme applied to unsteady one-dimensional advection, Comput. Methods Appl. Mech. Engrg 88 (1991) 17–74.

[11] D.K. Lilly, The representation of small-scale turbulence in numerical simulation experiments, in: Proc. of the IBM Scientific Computer Symposium on Environmental Sciences, 1967, pp. 195–210 (IBM Form No. 320-1951).

[12] D.K. Lilly, A proposed modification of the Germano subgrid-scale closure method, Phys. Fluids A 4 (3) (1992) 633–635.

[13] O. Métais, M. Lesieur, Spectral large-eddy simulation of isotropic and stably stratified turbulence, J. Fluid Mech 239 (1992) 157–194.

[14] P.D. Minev, F.N. van de Vosse, L.J.P. Timmermans, A.A. van Steenhoven, A second order splitting algorithm for thermally-driven flow problems, Int. J. Num. Meth. Heat Fluid Flow 6 (2) (1995) 51–60.

[15] P. Moin, J. Kim, Numerical investigation of turbulent channel flow, J. Fluid Mech 118 (1982) 341–377.

[16] P. Orlandi, Vortex dipole rebound from a wall, Phys. Fluids A 2 (8) (1990) 1429–1436.

[17] L. Pera, B. Gebhart, On the stability of laminar plumes some numerical solutions and experiments, Int. J. Heat Mass Transfer 14 (1971) 975–984.

[18] S.A. Piacsek, G.P. Williams, Conservation properties of convection difference schemes, J. Comp. Phys 6 (1970) 392–405.

[19] H. Rouse, C.S. Yih, H.W. Humphreys, Gravitational convection from a boundary source, Tellus 4 (1952) 201–210.

[20] J.S. Turner, Turbulent entrainment: the development of the entrainment assumption, and its application to geophysical flows, J. Fluid Mech 173 (1986) 431–471.

[21] G.J.F. van Heijst, J.B. Flór, Laboratory experiments on dipole structures in a stratified fluid, in: J.C.J. Nihoul, B.M. Jouart (Eds.), Mesoscale/Synoptic Coherent Structures in Geophysical Turbulence, Elsevier, Amsterdam, 1989, pp. 591–608.

[22] B. van Leer, Towards the ultimate conservative difference scheme. Part II: monotonicity and conservation combined in a second-order scheme, J. Comput. Phys 14 (1974) 361–370.

[23] V.C. Wong, D.K. Lilly, A comparison of two dynamic subgrid closure methods for turbulent thermal convection, Phys. Fluids 6 (2) (1994) 1016–1023.